Magnon valley thermal Hall effect in triangular-lattice antiferromagnets

Qi-Hui Chen [1,*] Fei-Jie Huang,[2] and Yong-Ping Fu[3]
[1]*School of Physical Science and Technology, Southwest Jiaotong University, Chengdu 610031, China*
[2]*Department of Physics, Kunming University, Kunming 650214, China*
[3]*Department of Physics, West Yunnan University, Lincang 677000, China*

(Received 31 March 2022; revised 22 May 2022; accepted 23 May 2022; published 1 June 2022)

We study the magnetic excitations of the antiferromagnetic XXZ model on two-dimensional triangular lattice. We find there is a magnon valley thermal Hall effect. As far as we know, this effect has been studied on only the ferromagnetic honeycomb lattice. We reveal that the valley thermal Hall conductivity also conforms to the universal behavior of thermal Hall conductivity proposed by Yang *et al.* [Phys. Rev. Lett. **124**, 186602 (2020)]. We derive a low-energy effective theory near the valleys and find that although the low-energy effective dynamic matrix is non-Hermitian, the Berry curvatures are mainly determined by its Hermitian part. We show that our results are general to some extent in the Y phase of the triangular lattice. By an explicit calculation with experimental parameters, we demonstrate that $Rb_4Mn(MoO_4)_3$ is a suitable material to realize the magnon valley thermal Hall effect.

DOI: 10.1103/PhysRevB.105.224401

I. INTRODUCTION

In electronic systems, valleytronics has received widespread attention because, in addition to charge and spin, it provides us with a new means of manipulating electrons [1,2]. The energy bands of two-dimensional materials with a honeycomb structure usually have two inequivalent valleys at the corners of the Brillouin zone. Therefore, current research on valleytronics mainly focuses on graphene or graphenelike materials, such as silicon and transition-metal dichalcogenides, $2H$-MX_2 [3–7]. The nonzero but opposite-sign Berry curvatures in the two valleys result in a valley-contrasting Hall transport, with carriers in different valleys turning into opposite directions perpendicular to an in-plane electric field. This phenomenon is called the valley Hall effect. It is similar to the Hall effect, in which the applied magnetic field exerts an opposite transverse Lorentz force on the moving positive and negative carriers and tends to push them to opposite sides of the conductor.

Investigations of topological matter in the electronic system have also been extended to theoretical predictions of topological magnon insulators [8–24]. Magnons are the elementary excitations of a magnetically ordered system which are ubiquitous in magnetic materials. With the breaking of inversion or time reversal symmetry, it is natural to expect the band structure of the magnon to show nontrivial topological properties. Based on the semiclassical equation of motion of magnons, it was shown that magnons exhibit a thermal Hall effect in which a temperature gradient leads to a transverse heat current [25]. The thermal Hall effect is characterized by transverse thermal Hall conductivity (TTHC) κ_{xy}, which is given as an integral of Berry curvature with a weight factor. However, in contrast to electronic systems, there are no quantized Hall plateaus because magnons are boson-obeying Bose-Einstein statistics. Therefore, the TTHC includes contributions from all the magnon bands. In experiments, the thermal Hall effect was first observed in the three-dimensional (3D) pyrochlore ferromagnetic insulators $Lu_2V_2O_7$, $Ho_2V_2O_7$, and $In_2Mn_2O_7$ [26,27]. Later, this effect was also reported in the two-dimensional kagome magnet Cu(1,3-bdc) [28,29].

The magnon valley thermal Hall effect (MVTHE) was also investigated recently [30–33]. Although the TTHCs are always zero in these systems, i.e., $\kappa_{xy} = 0$, the valley thermal Hall conductivity (VTHC) κ_{xy}^{v} is not zero. This means that a net pure valley Hall current can be created under a temperature gradient. Because of the opposite signs of the Berry curvatures between two inequivalent valleys, Zhai and Blanter pointed out that this effect can be detected by the inverse magnon valley Hall effect and valley Seebeck effect [31].

To the best of our knowledge, all the studies on the MVTHE have mainly focused on a lattice with honeycomb structure. In this work, we show that the MVTHE can also be realized in triangular lattice antiferromagnets. Our findings enlarge the class of magnetic crystals that exhibit the MVTHE. A large number of magnetic materials have been synthesized that realize triangular antiferromagnets, such as $Ba_3MnNb_2O_9$ [34], $Rb_4Mn(MoO_4)_3$ [35], $A_3NiNb_2O_9$ (with A=Ba, Sr and Ca) [36], $RbFe(MoO_4)_2$ [37], Cs_2CuBr_4 [38,39], Cs_2CuCl_4 [39–41], $Ba_3CoSb_2O_9$ [42–46], and κ-$(BEDT\text{-}TTF)_2Cu_2(CN)_3$ [BEDT-TTF is bis(ethylenedithio)tetrathiafulvalene] [47]. It is very promising that the predictions given in this paper are detected in experiment.

The remainder of this paper is organized as follows. In Sec. II, we introduce the XXZ spin model on a triangular lattice and discuss its classical phase diagram. In Sec. III, we first review the linear spin wave theory and then apply it to the

*qhchen@swjtu.edu.cn

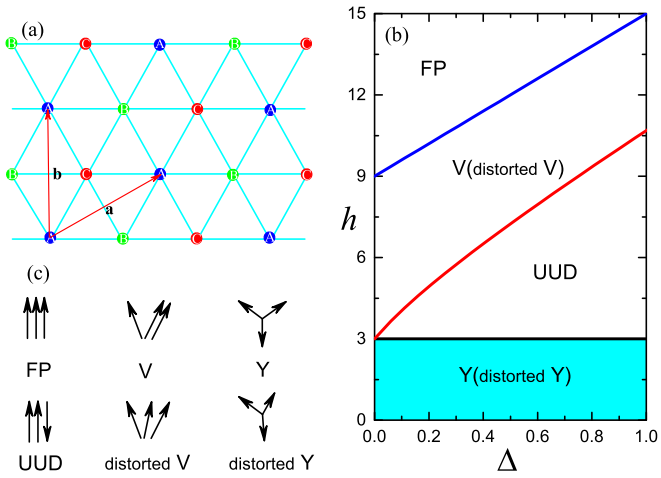

FIG. 1. (a) Triangular lattice with three sublattices denoted by A, B, and C. (b) The mean-field ground-state phase diagram of the XXZ spin model in Eq. (1) obtained in the classical limit ($S \to \infty$). There are four different regions whose spin configurations are given in (c). The arrows denote the spin orientations on the A, B, and C sublattices. When $\epsilon \neq 0$ and $\epsilon \ll 1$, Y and V phases will change to distorted Y and V, respectively. Because the change in the phase boundary is very small, we do not draw it here.

(distorted) Y phase shown in Fig. 1(c). Then the topological properties of the magnon band structures are investigated. We demonstrate that the MVTHE can be detected in this system. In Sec. IV, we establish a low-energy effective theory to further understand the topological properties of the system. In Sec. V, we show the material realization of the MVTHE in $Rb_4Mn(MoO_4)_3$. Finally, a discussion and conclusions are provided in Sec. VI.

II. HAMILTONIAN AND CLASSICAL PHASE DIAGRAM

For a theoretical work, we study the XXZ spin model on a triangular lattice with a magnetic field along the z axis,

$$H = \sum_{\langle i\alpha, j\beta\rangle} \left[J\mathbf{S}_{i\alpha}\cdot\mathbf{S}_{j\beta} + \Delta S^z_{i\alpha}S^z_{j\beta}\right] - \sum_{i\alpha} S h_\alpha S^z_{i\alpha}, \qquad (1)$$

where $\mathbf{S}_{i,\alpha}$ is the spin of magnitude S localized at the αth sublattice of the ith unit cell in a triangular lattice [see Fig. 1(a)]. $\alpha, \beta = A, B, C$ denote the three sublattices. $\langle\cdot,\cdot\rangle$ stands for the summation over nearest-neighbor lattice sites. The first term represents the magnetic exchange interaction with $J > 0$ for antiferromagnets. In the following discussion, we will choose the units of energy to be J, i.e., let $J = 1$. The second term with $\Delta > 0$ indicates the anisotropic exchange coupling. The last term is the applied magnetic field. We assume that h_α depends on the sublattice, which could be realized by a magnetic substrate.

First, we discuss the mean-field ground state of the model in Eq. (1), where the spins are viewed as classical vectors [48,49]. The spins on sublattice α are parameterized as

$$\mathbf{S}_\alpha = S(\sin\theta_\alpha\cos\phi_\alpha, \sin\theta_\alpha\sin\phi_\alpha, \cos\theta_\alpha). \qquad (2)$$

Without loss of generality, we set $\phi_\alpha = 0$ because of the invariance of the ground states under a uniform rotation of the azimuths. The energy of the mean-field Hamiltonian is described by three polar angles: $(\theta_A, \theta_B, \theta_C)$. Substituting Eq. (2) into Eq. (1), we obtain the mean-field energy per unit cell as

$$E_{\rm MF} = 3S^2 \sum_{(\alpha,\beta)} [(1+\Delta)\cos\theta_\alpha\cos\theta_\beta + \sin\theta_\alpha\sin\theta_\beta] - \sum_\alpha h_\alpha\cos\theta_\alpha, \qquad (3)$$

where the notation (α, β) means summation over the pairs of (A, B), (B, C), and (C, A). θ_α are determined by minimizing the energy E_{MF}. According to different solutions of θ_α, we identify different phases.

In this paper, we mainly focus on the phase diagram in the antiferromagnetic region ($\Delta > 0$), where four different phases are identified in a uniform applied magnetic field, i.e., $h_\alpha = h$. The phase diagram is shown in Fig. 1(b). This result is consistent with that obtained by Yamamoto *et al.* [50]. We use Griset's idiom to call these phases Y, V, up-up-down (UUD), and fully polarized (FP) phases [51]. The spin configurations of these states are plotted in Fig. 1(c). When $0 < h < 3$, the system is in the Y phase, with which we are mainly concerned. When $3 < h < h_{c1}$, the system will enter the UUD phase. The phase boundary between UUD and V can be worked out as $h_{c1} = \frac{3}{2}[1 + 2\Delta + \sqrt{1 + 12\Delta + 4\Delta^2}]$. When h is greater than h_{c1} but less than $h_{c2} = 9 + 2\Delta$, the system will enter the V phase. Finally, when $h > h_{c2}$, the system will be polarized fully. If we turn on a small deviation ϵ of the magnetic field on the B sublattice, i.e., $h_B = h + \epsilon$ and $\epsilon \ll 1$, the Y and V phases are replaced by distorted ones, as shown in Fig. 1(c).

III. TOPOLOGICAL MAGNON BAND

In this section, we first apply the linear spin wave theory to the model to introduce the concept of topological magnons. Then, through the band structure of the magnons, we define the TTHC and VTHC, which are related to the Berry curvature.

A. Linear spin wave theory

In linear spin wave theory, we need to perform a local rotation for the coordinate system at each lattice point, so that the mean-field directions of the spins point along the local z axis. Labeling the local frame spins as $\tilde{\mathbf{S}}_{i\alpha}$, the transformation between local and global spins is written as

$$\mathbf{S}_{i\alpha} = \begin{bmatrix} \cos\theta_\alpha & 0 & \sin\theta_\alpha \\ 0 & 1 & 0 \\ -\sin\theta_\alpha & 0 & \cos\theta_\alpha \end{bmatrix} \tilde{\mathbf{S}}_{i\alpha}. \qquad (4)$$

Finally, restricting ourselves to the harmonic excitation spectrum, we perform a truncated Holstein-Primakoff (HP) transformation:

$$\begin{aligned} \tilde{\mathbf{S}}^x_{i\alpha} &= \frac{\sqrt{S}}{2}(a^\dagger_{i\alpha} + a_{i\alpha}), \\ \tilde{\mathbf{S}}^y_{i\alpha} &= i\frac{\sqrt{S}}{2}(a^\dagger_{i\alpha} - a_{i\alpha}), \\ \tilde{\mathbf{S}}^z_{i\alpha} &= S - a^\dagger_{i\alpha}a_{i\alpha}, \end{aligned} \qquad (5)$$

with $a^{\dagger}_{i,\alpha}$ ($a_{i,\alpha}$) being a bosonic creation (annihilation) operator. Neglecting the terms of magnon-magnon interactions and performing the Fourier transformation, the Hamiltonian can be written in momentum space as

$$H = E_0 + \frac{S}{2}\sum_{\mathbf{k}} (\psi^{\dagger}(\mathbf{k}), \tilde{\psi}(-\mathbf{k}))\mathcal{H}(\mathbf{k})\begin{pmatrix}\psi(\mathbf{k})\\ \tilde{\psi}^{\dagger}(-\mathbf{k})\end{pmatrix}, \quad (6)$$

where E_0 is the total energy of the mean-field ground state, $\psi^{\dagger}(\mathbf{k}) = (a^{\dagger}_{\mathbf{k}A}, a^{\dagger}_{\mathbf{k}B}, a^{\dagger}_{\mathbf{k}C})$, and the tilde over ψ means the transpose operation. The bosonic Bogoliubov Hamiltonian $\mathcal{H}(\mathbf{k})$ has the following form:

$$\mathcal{H}(\mathbf{k}) = \begin{bmatrix}\mathcal{A}(\mathbf{k}) & \mathcal{B}(\mathbf{k})\\ \mathcal{B}^{\star}(-\mathbf{k}) & \mathcal{A}^{\star}(-\mathbf{k})\end{bmatrix}. \quad (7)$$

If we define the quantities

$$\begin{aligned} Y^{\pm}_{\alpha\beta} &= \cos(\theta_\alpha - \theta_\beta) + \Delta \sin\theta_\alpha \sin\theta_\beta \pm 1,\\ X_{\alpha\beta} &= 3\cos(\theta_\alpha - \theta_\beta) + 3\Delta \cos\theta_\alpha \cos\theta_\beta, \end{aligned} \quad (8)$$

the diagonal and off-diagonal elements of the matrices $\mathcal{A}(\mathbf{k})$ and $\mathcal{B}(\mathbf{k})$ are given by

$$\begin{aligned} [\mathcal{A}(\mathbf{k})]_{\alpha\alpha} &= h_\alpha \cos\theta_\alpha - \sum_{\beta\neq\alpha} X_{\alpha\beta},\\ [\mathcal{A}(\mathbf{k})]_{\alpha\beta} &= Y^{+}_{\alpha\beta}\Gamma_{\alpha\beta}(\mathbf{k}),\\ [\mathcal{B}(\mathbf{k})]_{\alpha\alpha} &= 0,\\ [\mathcal{B}]_{\alpha\beta} &= Y^{-}_{\alpha\beta}\Gamma_{\alpha\beta}(\mathbf{k}), \end{aligned} \quad (9)$$

where $\Gamma_{\alpha\beta}(\mathbf{k})$ is defined by the following sum:

$$\Gamma_{\alpha\beta}(\mathbf{k}) = \frac{1}{2}\sum_{\delta} \exp(i\mathbf{k}\cdot\boldsymbol{\delta}), \quad (10)$$

where it is worth noting that the sum is over nearest-neighbor vectors $\boldsymbol{\delta}$ connecting an α sublattice site to a β sublattice site. Due to the conservation of the effective time reversal symmetry (ETRS) [18], it is easy to show that $\mathcal{A}(\mathbf{k}) = \mathcal{A}^{\star}(-\mathbf{k})$ and $\mathcal{B}(\mathbf{k}) = \mathcal{B}^{\star}(-\mathbf{k})$. For a coplanar spin texture, if $\hat{e}$ is a unit vector perpendicular to this plane, the ETRS indicates the invariance of the spin texture under a combination of actual time reversal and a spin rotation by π about $\hat{e}$.

The Hamiltonian (6) is diagonalized by a paraunitary Bogoliubov transformation [52], which amounts to finding a matrix $T_{\mathbf{k}}$ such that

$$T^{\dagger}_{\mathbf{k}}\mathcal{H}_{\mathbf{k}}T_{\mathbf{k}} = \mathcal{E}_{\mathbf{k}}, \quad T^{\dagger}_{\mathbf{k}}\Lambda T_{\mathbf{k}} = \Lambda, \quad (11)$$

where $\Lambda = \mathrm{diag}(1,1,1,-1,-1,-1)$ and $\mathcal{E}_{\mathbf{k}} = \mathrm{diag}(\epsilon_{1,\mathbf{k}}, \epsilon_{2,\mathbf{k}}, \epsilon_{3,\mathbf{k}}, \epsilon_{1,-\mathbf{k}}, \epsilon_{2,-\mathbf{k}}, \epsilon_{3,-\mathbf{k}})$ gives the three magnon energy bands. The second formula in Eq. (11) ensures the bosonic commutation rule of the magnons. The magnon bands are shown in Fig. 2 for $h < 3$, where the system locates in the Y (distorted Y) phase. In this paper, we consider only the case where the magnetic field on the B sublattice has a small deviation ϵ from the uniform magnetic field h. From the left (or right) column of Fig. 2, we can see that as Δ increases, the separation of the uppermost band from the lowest two bands becomes larger and larger. Thus, we can focus on only the lowest two bands near the K and K' points at low temperature and large Δ. In a uniform magnetic field with $\epsilon = 0$, the system is in the Y phase, and the two lowest magnon bands touch at K and K', forming massless Dirac-cone-like dispersions. We can work out the mean-field ground state with $\theta_{A,0} = \pi$, $\theta_{B,0} = -\theta_{C,0} = \theta$, where

$$\theta = \arccos\left(\frac{3\Delta + h + 3}{3\Delta + 6}\right) \quad (12)$$

is obtained by minimizing the mean-field energy in Eq. (3).

When ϵ is turned on, the system will enter the distorted Y phase, and the Dirac-cone-like dispersions are gapped due to the breaking of the mirror symmetry. The mirror symmetry is defined as the system remains unchanged when the spins on the B and C sublattices are exchanged. Because the ϵ considered here is small, we can expand the mean-field ground-state solutions of θ_α to the first order of ϵ, which are written as $\theta_\alpha \approx \theta_{\alpha,0} + \Delta_\alpha\epsilon$. The expansion coefficients Δ_α as a function of h and Δ are shown in Fig. 3. The method to calculate those coefficients is given in Appendix A. In order to demonstrate the effectiveness of this expansion, we also show a comparison of θ_α obtained with the exact numerical method and the expansion method in the insets in Fig. 3. We find that the larger Δ is, the more accurate the expansion is. The gap between the lowest two bands at the K and K' points can be written, up to first order of ϵ, as

$$\Delta_{\mathrm{gap}} = \epsilon\{\cos\theta + [6\Delta_A - (3 + 3\Delta + h)(\Delta_B + \Delta_C)]\sin\theta\}, \quad (13)$$

where θ is determined by Eq. (12).

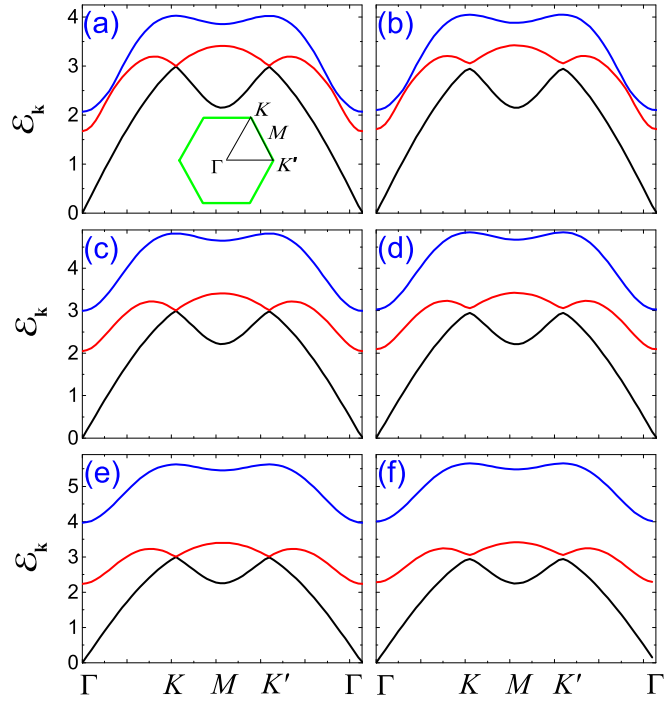

FIG. 2. The magnon bands of the XXZ spin model on a triangular lattice at $h = 1.1$. (a) $\Delta = 0.2, \epsilon = 0$. (b) $\Delta = 0.2, \epsilon = 0.05$. (c) $\Delta = 0.35, \epsilon = 0$. (d) $\Delta = 0.35, \epsilon = 0.05$. (e) $\Delta = 0.5, \epsilon = 0$. (f) $\Delta = 0.5, \epsilon = 0.05$. The inset in (a) sketches the first Brillouin zone of the triangular lattice.

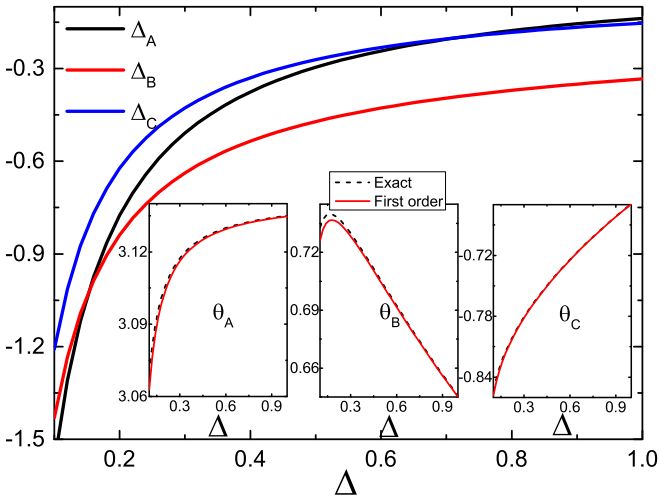

FIG. 3. The expansion coefficients Δ_α with $\alpha = A, B, C$ at $h = 1.1$. The insets give the mean-field ground-state solutions of θ_α obtained with the exact numerical method (dashed black lines) and the expansion method up to first order of ϵ (solid red lines).

B. Magnon valley thermal Hall conductivity

The Berry curvature of the nth magnon band is defined as [11]

$$\Omega_n(\mathbf{k}) = i\varepsilon_{\mu\nu}\left[\Lambda\partial_{k_\mu}T_{\mathbf{k}}^\dagger\Lambda\partial_{k_\nu}T_{\mathbf{k}}\right]_{nn}, \tag{14}$$

where $\varepsilon_{\mu\nu}$ is the second-order antisymmetric tensor, where $\mu, \nu = x, y$ and the Einstein summation convention has been used for this index, and $[M]_{nn}$ is the nth diagonal element of the matrix M. Since the phase of the wave function was uncertain in the numerical diagonalization, Eq. (14) is not suitable for the numerical calculation. Thus, we adopt the gauge-invariant form of the Berry curvature,

$$\Omega_n(\mathbf{k}) = -2\mathrm{Im}\sum_{m\neq n}^{2N}\frac{\left[\Lambda T_{\mathbf{k}}^\dagger(\partial_{k_x}\mathcal{H}_{\mathbf{k}})T_{\mathbf{k}}\right]_{nm}\left[\Lambda T_{\mathbf{k}}^\dagger(\partial_{k_y}\mathcal{H}_{\mathbf{k}})T_{\mathbf{k}}\right]_{mn}}{([\Lambda\mathcal{E}_{\mathbf{k}}]_{nn}-[\Lambda\mathcal{E}_{\mathbf{k}}]_{mm})^2}. \tag{15}$$

It can be confirmed that Eq. (14) is equivalent to Eq. (15). Figure 4 shows the Berry curvatures of magnon bands in Fig. 2(f). As shown in Fig. 4(c), the Berry curvature for the top band is almost zero in the whole Brillouin zone. Therefore, the contribution of the top band to the valley thermal Hall effect can be ignored. From Figs. 4(a) and 4(b), we can see that the nonzero Berry curvature is mainly concentrated at the K and K' points for the middle and bottom bands.

Using linear response theory, Matsumoto *et al.* [11] derived the TTHC as

$$\kappa_{xy} = -\frac{k_B^2T}{\hbar V}\sum_{\mathbf{k}}\sum_{n=1}^{N}\left\{c_2[g(\epsilon_{n,\mathbf{k}})]-\frac{\pi^2}{3}\right\}\Omega_{n\mathbf{k}}, \tag{16}$$

where k_B is the Boltzmann constant, T is temperature, $\hbar$ is the Plank constant, V is the volume of the system, N is the number of sublattices, $g(\epsilon_{n,\mathbf{k}}) = [e^{\epsilon_{n,\mathbf{k}}/k_BT}-1]^{-1}$ is the bosonic distribution function, $c_2(x) = (1+x)(\ln\frac{1+x}{x})^2 - (\ln x)^2 - 2\mathrm{Li}_2(-x)$, $\mathrm{Li}_2(x)$ is the dilogarithm, and the sum for $\mathbf{k}$ is over the first Brillouin zone.

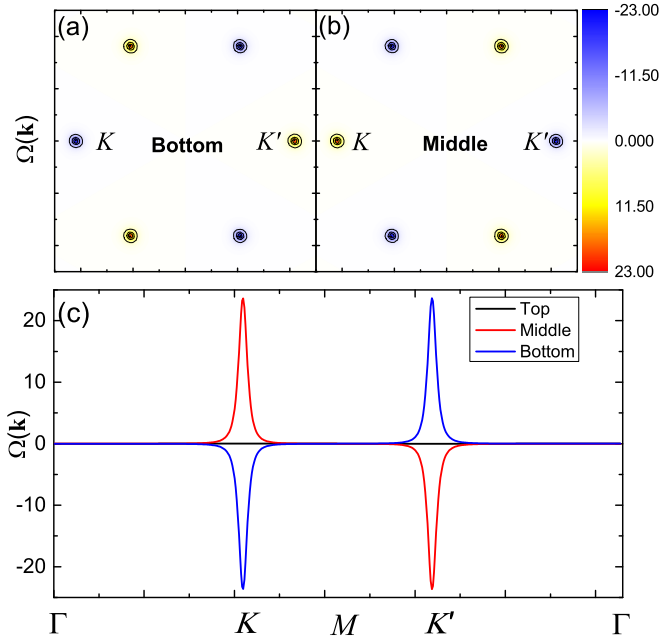

FIG. 4. Berry curvatures in the $\mathbf{k}$ plane for the (a) bottom and (b) middle bands. (c) The Berry curvatures for three bands along the Γ-K'-M-K-Γ line as shown in Fig. 2(a). The parameters are the same as in Fig. 2(f). Here, we assume that the lattice constant is unit.

Because of the ETRS, it can be shown that the Berry curvature of the single-magnon band is an odd function with respect to momentum $\mathbf{k}$, i.e., $\Omega_n(\mathbf{k}) = -\Omega_n(-\mathbf{k})$ [18]. This is confirmed by our numerical results in Figs. 4(a) and 4(b). Consequently, if we put an odd $\Omega_n(\mathbf{k})$ into Eq. (16), we find that $\kappa_{xy} = 0$ because the contributions from $\mathbf{k}$ and $-\mathbf{k}$ cancel each other. However, a pure valley current of magnons is generated.

The semiclassical equations of motion of magnons [25,53] are given as

$$\dot{\mathbf{r}}_n = \frac{1}{\hbar}\frac{\partial\epsilon_{n,\mathbf{k}}}{\partial\mathbf{k}} - \dot{\mathbf{k}}\times\hat{z}\Omega_n(\mathbf{k}), \quad \hbar\dot{\mathbf{k}} = -\nabla U(\mathbf{r}), \tag{17}$$

where $\mathbf{r}_n$ denotes the location of the magnon wave packet constructed by the nth band, $\hat{z}$ is the out-of-plane unit vector, and $U(\mathbf{r})$ is a slowly varying potential for the magnons, which may result from the nonuniform distribution of the temperature. According to the second term in the first equation in Eq. (17), the nonzero but opposite-sign Berry curvatures in the two valleys can result in a valley-contrasting magnon transport. The magnons in different valleys turn in opposite directions perpendicular to the in-plane temperature gradient ∇T. This is the origin of the MVTHE. The VTHC is defined as [31]

$$\kappa_{xy}^v = -\frac{k_B^2T}{\hbar V}\sum_{\mathbf{q}}\sum_{n=1}^{N}C_n(\mathbf{q})\left(\Omega_{n\mathbf{q}}^K-\Omega_{n\mathbf{q}}^{K'}\right), \tag{18}$$

where $C_n(\mathbf{q}) \equiv \{c_2[g(\epsilon_{n,\mathbf{q}})]-\frac{\pi^2}{3}\}$ and $\mathbf{q} \equiv \mathbf{k} - K$ (K') is defined around the K (K') valley. It is worth noting that the summation over $\mathbf{q}$ around K (K') runs over only half of the first Brillouin zone.

We show the results of the calculation of the VTHC κ_{xy}^v in Fig. 5. The trends of the VTHC as a function of temperature

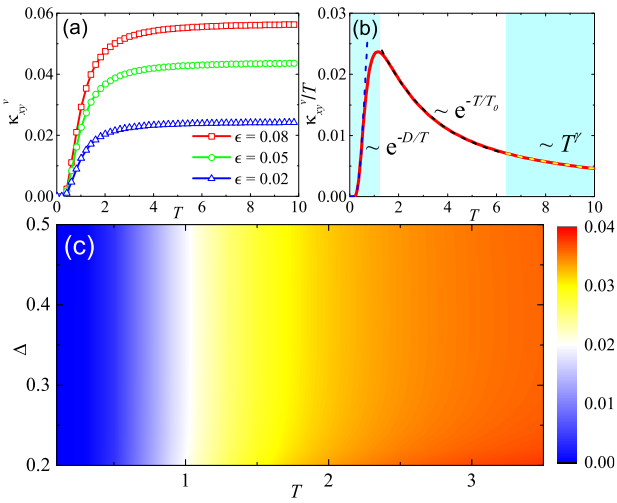

FIG. 5. The valley thermal Hall conductivity κ_{xy}^{v} for different ϵ values in (a), where $\Delta = 0.5, h = 1.1$. (b) The universal behavior of κ_{xy}^{v}/T vs T; the solid red line is the exact numerical result, and the dashed lines in different regions denote the theoretical fits with the different fitting functions shown. The parameters are $\Delta = 0.5, h = 1$, and $\epsilon = 0.05$. (c) Contour plot of κ_{xy}^{v} in T and the Δ plane with $h = 1, \epsilon = 0.05$. Here, we set the lattice constant to be the unit length and $k_B = \hbar = 1$.

T are shown in Fig. 5(a) for several values of ϵ with fixed $\Delta = 0.5, h = 1.1$. It is demonstrated that the VTHC increases with ϵ at the same temperature. In Fig. 5(b), it is shown that κ_{xy}^{v}/T also conforms to the universal behavior given by Yang *et al.* for bosons [54]. At $T = 0, \kappa_{xy}^{v}/T$ vanishes, and at low temperature it grows as $\sim e^{-D/T}$, where D is a fitting constant. At the intermediate temperature, κ_{xy}^{v}/T decreases with an exponential form $\sim e^{T/T_0}$. Finally, the VTHC approaches a constant value for very large temperature, or, equivalently, $\kappa_{xy}^{v}/T \sim T^{\gamma}$ in the high-T limit with $\gamma = 1$ for magnons. The contour plot of κ_{xy}^{v} in Fig. 5(c) shows that VTHC changes only slightly with the variation of Δ in the range of $0.2 < \Delta < 0.5$.

IV. THE LOW-ENERGY EFFECTIVE THEORY

According to Figs. 4(a) and 4(b), we see that the nonzero Berry curvatures mainly concentrate around the K and K' valleys. In order to gain a deeper understanding of the topological properties of the system, in this section we derive the low-energy effective theory near the valleys.

It can be proved that the contribution of the uppermost energy band near the valleys in Fig. 2 mainly comes from the A sublattice. Therefore, we ignore the A sublattice under the low-energy approximation. It is worth noting that the remaining lattice points constitute a honeycomb lattice. This explains why there is valley physics in a triangular lattice. In addition, we regard both $\mathbf{q}$ and ϵ as small quantities, i.e., $q, \epsilon \ll 1$. By expanding the Hamiltonian to linear order in $\mathbf{q}, \epsilon$ near the K point, the effective Hamiltonian can be written as

$$H_K^{\text{eff}} = \mathcal{G}\tau_0 \otimes \sigma_0 + \tau_{\text{eff}} \otimes \boldsymbol{\sigma} \cdot \mathbf{q} + m\tau_0 \otimes \sigma_z, \tag{19}$$

and near K' point, it is

$$H_{K'}^{\text{eff}} = \mathcal{G}\tau_0 \otimes \sigma_0 + \tau'_{\text{eff}} \otimes \boldsymbol{\sigma}' \cdot \mathbf{q} + m\tau_0 \otimes \sigma_z, \tag{20}$$

where $\tau_{\text{eff}} = \mathcal{F}\tau_0 + \mathcal{D}\tau_x$, $\tau'_{\text{eff}} = -\tau_{\text{eff}}$, $\boldsymbol{\sigma} = \{\sigma_x, \sigma_y\}$, and $\boldsymbol{\sigma}' = \sigma_x\boldsymbol{\sigma}\sigma_x$. Here, τ_0 and $\{\tau_x, \tau_y, \tau_z\}$ are a 2×2 identity matrix and the Pauli matrices, respectively, which come from the nonconservation of the particle number of the antiferromagnetic HP transformation. And σ_0 and $\{\sigma_x, \sigma_y, \sigma_z\}$ are also a 2×2 identity matrix and the Pauli matrices, which denote the B and C sublattices. $\mathcal{G}, \mathcal{D}, \mathcal{F}, m$ are constants determined by the original model parameters in Eq. (1). These parameters are derived in Appendix B up to the first-order approximation of ϵ.

It is worth noting that the constant diagonal matrices (first term) in Eqs. (19) and (20) cannot be eliminated by energy translation. Because the diagonalizing method discussed in Eq. (11) is equivalent to the diagonalizing of the dynamic Hamiltonian, i.e., $(\tau_z \otimes \sigma_0)H^{\text{eff}}$, the constant term in H^{eff} is not a constant diagonal matrix in the dynamic Hamiltonian. In general, the dynamic Hamiltonian is a non-Hermitian matrix unless $\mathcal{D} = 0$.

Now, we consider $\mathcal{G} = 1$ and $\mathcal{D}, \mathcal{F}$, and m as free parameters to study the properties of the effective Hamiltonian when $\mathbf{q}$ is small. Since $H_{K'}^{\text{eff}}$ can be obtained from H_K^{eff} by the transformation $\{q_x, q_y\} \to \{-q_x, q_y\}$, we focus on only the properties of H_K^{eff}.

A. $\mathcal{D} = 0$

As we have already pointed out, in this case, the dynamic matrix of H_K^{eff} becomes Hermitian and can be written as

$$H_{K,D}^{\text{eff}} = \tau_z \otimes [\sigma_0 + \mathcal{F}\boldsymbol{\sigma} \cdot \mathbf{q} + m\sigma_z] \equiv \tau_z \otimes H_\sigma^{\text{eff}}. \tag{21}$$

This is a block-diagonal matrix and is easy to diagonalize. If we denote the eigenstates of τ_z and H_σ^{eff} as $\{|+_\tau\rangle, |-_\tau\rangle\}$ and $\{|+_\sigma\rangle, |-_\sigma\rangle\}$, respectively, then the eigenstates of $H_{K,D}^{\text{eff}}$ can be obtained as $\{|+_\tau +_\sigma\rangle, |+_\tau -_\sigma\rangle, |-_\tau +_\sigma\rangle, |-_\tau -_\sigma\rangle\}$. The eigenvalues of $H_{K,D}^{\text{eff}}$ are $\{E_+, E_-, -E_+, -E_-\}$, where $E_\pm = 1 \pm \sqrt{\mathcal{F}^2q^2 + m^2}$, with $q = \sqrt{q_x^2 + q_y^2}$ satisfying $H_\sigma^{\text{eff}}|+_\sigma\rangle = E_+|+_\sigma\rangle, H_\sigma^{\text{eff}}|-_\sigma\rangle = E_-|-_\sigma\rangle$. Then we can show that the Berry curvature given in Eq. (15) can be reduced to the one defined in the particle-conserving system, which is written as

$$\Omega_n(\mathbf{q}) = -2\text{Im}\sum_{m\neq n} \frac{\langle n_\sigma|\left(\partial_{q_x}H_\sigma^{\text{eff}}\right)|m_\sigma\rangle\langle m_\sigma|\left(\partial_{q_y}H_\sigma^{\text{eff}}\right)|n_\sigma\rangle}{(E_n - E_m)^2}, \tag{22}$$

where $m, n = +, -$. In this case, we can analytically determine the Berry curvature as

$$\Omega_\pm(\mathbf{q}) = \mp\frac{\mathcal{F}^2 m}{2\Delta_{\mathbf{q}}^3}, \tag{23}$$

where $\Delta_{\mathbf{q}} \equiv \sqrt{\mathcal{F}^2q^2 + m^2}$. So we see that when $q \to 0$, $\Omega_\pm \sim \mp\frac{\mathcal{F}^2}{m^2}$. According to Eq. (17), this equation tells us how to increase the lateral velocity of the magnon near the valleys.

B. $\mathcal{D} \neq 0$

In this case, the dynamic matrix of H_K^{eff} is a non-Hermitian matrix,

$$H_{K,D}^{\text{eff}} = \mathcal{G}\tau_z \otimes \sigma_0 + \tilde{\tau}_{\text{eff}} \otimes \boldsymbol{\sigma} \cdot \mathbf{q} + m\tau_z \otimes \sigma_z, \tag{24}$$

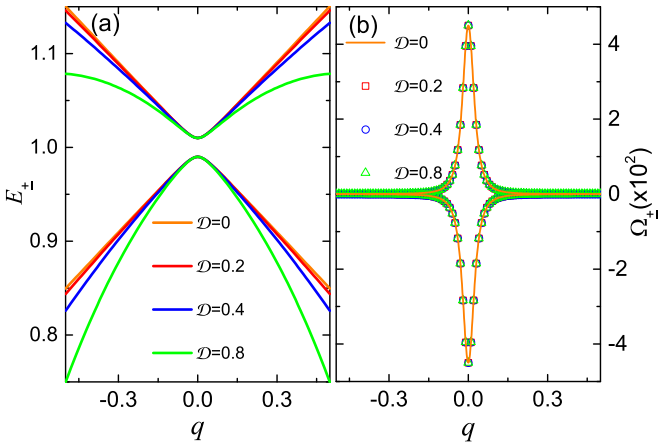

FIG. 6. (a) The energy bands and (b) the Berry curvature of different values of $\mathcal{D}$ for the low-energy effective Hamiltonian H_K^{eff}. The scattering lines in (b) are the results of numerical calculation, and the solid orange line is given by Eq. (23). The parameters are $\mathcal{F} = 0.3$ and $m = 0.01$.

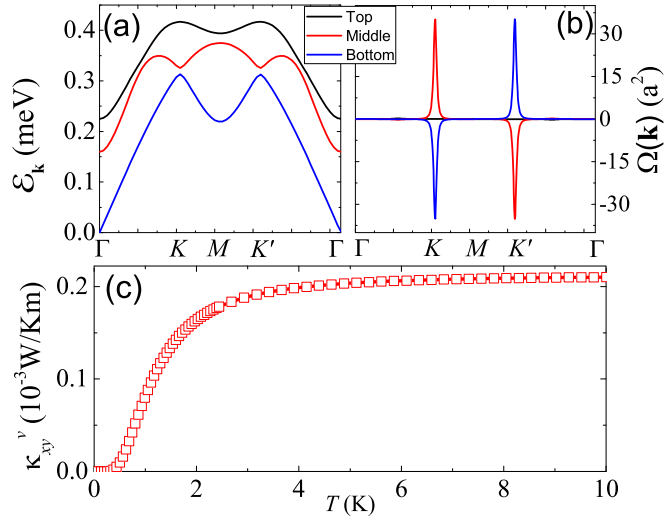

FIG. 7. (a) The magnon bands, (b) the Berry curvatures, and (c) the VTHC κ_{xy}^{v} for $Rb_4Mn(MoO_4)_3$. According to the experiment [35], the parameters are given as $\tilde{J} = 0.11$ meV, $D = 0.22\tilde{J}$, $a = 6.099$ Å, $B_A = B_C = 1.045$ T, and $B_B = 1.093$ T.

with $\tilde{\tau}_{\text{eff}} = \mathcal{F}\tau_z + i\mathcal{D}\tau_y$. As long as the values of $\mathcal{D}$ and q are not too large, the eigenvalues of $H_{K,D}^{\text{eff}}$ are still real. In the following, we will always assume that this condition holds, as the low-energy effective theory is derived from self-consistent spin wave theory.

The energy bands and Berry curvatures of the effective Hamiltonian H_K^{eff} are shown in Fig. 6. By numerical calculations, we find that the Berry curvatures are hardly affected by $\mathcal{D}$. As shown in Fig. 6(b), their values are almost identical to those given by Eq. (23). This means that the VTHC κ_{xy}^{v} of the system mainly depends on the Hermitian part of the dynamic matrix $H_{K,D}^{\text{eff}}$. It can be understood by using perturbation theory. If we treat q and $\mathcal{D}$ as small quantities, up to $\mathcal{D}^2q^2$ order, we work $\Omega_{\pm}(\mathbf{q})$ out as

$$\Omega_{\pm}(\mathbf{q}) = \mp\frac{m}{2\Delta_{\mathbf{q}}^3}\left[\mathcal{F}^2 - \mathcal{D}^2m^2 + q^2\mathcal{D}^2\mathcal{F}^2\left(1 + \frac{m^2}{2\Delta_{\mathbf{q}}^2}\right)\right]. \tag{25}$$

When $q \to 0$, because $m \sim \epsilon \ll 1$, by comparing with Eq. (23), it is clear that the contributions of the correction terms in Eq. (25) are very small. We find that the perturbation is valid even when $\mathcal{D}$ reaches the order of 1.

V. MATERIAL REALIZATION

There are some materials described by the XXZ model on the triangular lattice but with $-1 < \Delta < 0$, such as $Ba_3CoSb_2O_9$ [42–46] and $A_3NiNb_2O_9$, with A=Ba, Sr, and Ca [36]. To the best of our knowledge, although there are still no experimental reports on the discovery of materials with $\Delta > 0$, many materials with the Y phase have been found and provide the possibility to observe the effect discussed in this paper. These materials include $Ba_3MnNb_2O_9$ [34], $Rb_4Mn(MoO_4)_3$ [35], and $Ba_3CoSb_2O_9$ [55].

In fact, we find that our results are general to some extent for the Y phase on the triangular lattice. Therefore, the expected order of magnitude for the VTHC can be obtained in real materials, such as $Rb_4Mn(MoO_4)_3$, which is a quasi-two-dimensional easy-axis triangular antiferromagnet with $S = \frac{5}{2}$. The intralayer and interlayer distances between Mn^{2+} ions are given by $a = 6.099$ Å and $c/2 = 11.856$ Å, respectively. The Hamiltonian describing $Rb_4Mn(MoO_4)_3$ is given by $H = \tilde{J}\sum_{ij}\mathbf{S}_i \cdot \mathbf{S}_j - D\sum_i (S_i^z)^2 - g\mu_B\sum_i BS_i^z$, with $D > 0$ [35]. We assume that the magnetic field is applied along the c axis. The strength of the intralayer exchange interaction and the single-ion anisotropy are obtained by experiment as $\tilde{J} = 1.2$ K ≈ 0.11 meV and $D = 0.22\tilde{J}$, respectively [35].

The system locates in the Y phase when the magnetic field is small. The magnon bands, the corresponding Berry curvatures, and the VTHC are shown in Figs. 7(a)–7(c), respectively. We have assumed that the applied magnetic fields in the three sublattice are $B_A = B_C = 1.045$ T and $B_B = 1.093$ T.

By comparing Fig. 7 with Figs. 2, 4, and 5, it is found the MVTHE discussed for the XXZ model can also be realized in the Y phase of $Rb_4Mn(MoO_4)_3$. Furthermore, around $T = 8$ K, κ_{xy}^{v} reaches 0.2×10^{-3} W/Km, which is the order of magnitude that can be detected experimentally [26].

VI. DISCUSSION AND CONCLUSIONS

In experiments, as Zhai and Blanter discussed, the MVTHE can be detected using the inverse magnon valley Hall effect and valley Seebeck effect [31]. There are still no experimental reports on the discovery of materials described by the XXZ model with $\Delta > 0$. On the other hand, cold atoms in an optical lattice have received more and more attention due to their high degree of controllability [56,57]. Many ways to implement the spin model have also been proposed [58,59] for optical lattices. We note that there are also some schemes to implement the XXZ model in the triangular optical lattice [60]. Therefore, we hope that this study will attract the attention of both the materials and cold-atom physics fields.

In summary, we have studied the magnetic excitation of the antiferromagnetic XXZ model on a two-dimensional triangular lattice. We found that, in the Y phase, there are Dirac-cone-like band structures for the magnon excitations located in two inequivalent valleys of the hexagonal Brillouin zone. This is a system capable of providing this kind of band structure, unlike previous studies on graphene or graphenelike materials. We point out that the energy degeneracy at the Dirac points can be removed by a sublattice-dependent magnetic field. Due to the nonzero and opposite signs of the Berry curvatures in the two valleys, a valley thermal Hall effect can be created in this system. By calculating the VTHC κ_{xy}^{v}, we found that κ_{xy}^{v}/T conforms the universal behaviors proposed by Yang *et al.* In order to deeply understand the topological properties of the system, we also derived a low-energy effective theory near the valley. We found that although the low-energy effective dynamic matrix is non-Hermitian, the VTHC κ_{xy}^{v} is mainly determined by its Hermitian part. We also showed that our results are general to some extent in the Y phase. By an explicit calculation using the experimental parameters of $Rb_4Mn(MoO_4)_3$, we demonstrated that it is a suitable material for realizing the MVTHE, and we gave an estimation of the expected order of magnitude for the VTHC. Our results suggest a number of future theoretical and experimental directions that will be useful for understanding the magnon excitation properties of triangular-lattice antiferromagnets.

ACKNOWLEDGMENTS

Q.-H.C. is supported by the National Natural Science Foundation of China (Grant No.12147208) and the Science and Technology Department of Sichuan Province (Grant No. 2020YFSY0016). F.-J.H. acknowledges support from the Yunnan Local Colleges Applied Basic Research Projects (Grant No. 2017FH001-112). Y.-P.F. acknowledges support from the National Natural Science Foundation of China (Grant No.11805029).

APPENDIX A: THE CALCULATION OF THE EXPANSION COEFFICIENTS Δ_α

In this Appendix, we discuss how to calculate the expansion coefficients Δ_α of mean-field solutions for θ_α, with $\alpha = A, B, C$. As we discussed in the main text, when $\epsilon = 0$, the solutions of θ_α can be worked out as $\theta_{A,0} = \pi, \theta_{B,0} = -\theta_C = \theta$, with $\theta = \arccos(3(\Delta + h + 3)/(3\Delta + 6)$. When $\epsilon \neq 0$ and is small, we denote the mean-field energy $E_{\mathrm{MF}}(\theta_A, \theta_B, \theta_C)$ as $E_{\mathrm{MF}}(\pi + \epsilon_A, \theta + \epsilon_B, -\theta + \epsilon_C) \equiv \tilde{E}_{\mathrm{MF}}(\epsilon_A, \epsilon_B, \epsilon_C, \epsilon)$. Here, ϵ_A, ϵ_B, and ϵ_C are the small changes in θ_A, θ_B, and θ_C induced by ϵ, respectively, which not only depend on the value of ϵ but are also related to the model parameters parameters J, h, and Δ. Up to first order of ϵ, we can obtain $\epsilon_\alpha \approx \Delta_\alpha \epsilon$. According to the minimum condition of the mean-field ground-state energy, ϵ_A, ϵ_B, ϵ_C are

$$\begin{aligned}
\frac{\partial \tilde{E}_{\mathrm{MF}}}{\partial \epsilon_A} &\equiv g_A(\epsilon, \epsilon_A, \epsilon_B, \epsilon_C) = 0,\\
\frac{\partial \tilde{E}_{\mathrm{MF}}}{\partial \epsilon_B} &\equiv g_B(\epsilon, \epsilon_A, \epsilon_B, \epsilon_C) = 0,\\
\frac{\partial \tilde{E}_{\mathrm{MF}}}{\partial \epsilon_C} &\equiv g_C(\epsilon, \epsilon_A, \epsilon_B, \epsilon_C) = 0.
\end{aligned} \tag{A1}$$

Equation (A1) is a set of nonlinear equations which are difficult to solve. However, we know the exact solution is $\epsilon_A = \epsilon_B = \epsilon_C = 0$ when $\epsilon = 0$, i.e., $g_\alpha(\mathbf{0}) = 0$. Since ϵ is a small, we treat ϵ_α as a function of ϵ and expand Eq. (A1) into a Taylor series of ϵ and obtain

$$\begin{aligned}
g_A(\mathbf{0}) + \frac{dg_A(\mathbf{0})}{d\epsilon}\epsilon + o(\epsilon) = 0,\\
g_B(\mathbf{0}) + \frac{dg_B(\mathbf{0})}{d\epsilon}\epsilon + o(\epsilon) = 0,\\
g_C(\mathbf{0}) + \frac{dg_C(\mathbf{0})}{d\epsilon}\epsilon + o(\epsilon) = 0.
\end{aligned} \tag{A2}$$

Up to first order of ϵ, we require $\frac{dg_\alpha(\mathbf{0})}{d\epsilon} = 0$ because $g_\alpha(\mathbf{0}) = 0$. If we denote $\frac{\partial g_\alpha}{\partial \epsilon_\beta}(\mathbf{0}) \equiv g_{\alpha\beta}$ and $\frac{\partial g_\alpha}{\partial \epsilon}(\mathbf{0}) \equiv g_{\alpha\epsilon}$, then we have

$$\begin{aligned}
g_{AA}\Delta_A + g_{AB}\Delta_B + g_{AC}\Delta_C = -g_{A\epsilon},\\
g_{BA}\Delta_A + g_{BB}\Delta_B + g_{BC}\Delta_C = -g_{B\epsilon},\\
g_{CA}\Delta_A + g_{CB}\Delta_B + g_{CC}\Delta_C = -g_{C\epsilon},
\end{aligned} \tag{A3}$$

where $g_{AA} = -h + 6(1 + \Delta)\cos(\theta)$, $g_{BB} = g_{CC} = (3 + h + 3\Delta)\cos(\theta) - 3(1 + \Delta)\cos^2(\theta) + 3$, $g_{AB} = g_{BA} = g_{AC} = g_{CA} - 3\cos(\theta)$, $g_{BC} = g_{CB} = 3(2 + \Delta)\cos^2(\theta) - 3(1 + \Delta)$, and $g_{A\epsilon} = g_{C\epsilon} = 0$, $g_{B\epsilon} = -\sin(\theta)$. By solving Eq. ((A3)), we obtain

$$\begin{aligned}
\Delta_A &= \frac{-g_{AB}g_{B\epsilon}}{2g_{AB}^2 - g_{AA}g_{BB} - g_{AA}g_{BC}},\\
\Delta_B &= \frac{\left(g_{AA}g_{BB} - g_{AB}^2\right)g_{B\epsilon}}{(g_{BB} - g_{BC})\left(2g_{AB}^2 - g_{AA}g_{BB} - g_{AA}g_{BC}\right)},\\
\Delta_C &= \frac{\left(g_{AB}^2 - g_{AA}g_{BC}\right)g_{B\epsilon}}{(g_{BB} - g_{BC})\left(2g_{AB}^2 - g_{AA}g_{BB} - g_{AA}g_{BC}\right)}.
\end{aligned} \tag{A4}$$

APPENDIX B: THE RELATIONS BETWEEN $\mathcal{G}$, $\mathcal{D}$, $\mathcal{F}$, AND m AND THE ORIGINAL MODEL PARAMETERS

In order to obtain the low-energy effective Hamiltonian, we first expand the Hamiltonian (7) as a power series of ϵ and keep only first-order terms, i.e., $\mathcal{H}(\mathbf{k}) = \mathcal{H}_0 + \epsilon\mathcal{H}_1$. Then we ignore the matrix elements related to the A sublattice under the low-energy approximation. These steps require us to expand $Y_{\alpha\beta}^{\pm}$ and $[\mathcal{A}(\mathbf{k})]_{\alpha\alpha} \equiv \mathcal{A}_{\alpha\alpha}$ into a series of ϵ and keep the first-order terms. The definitions of $Y_{\alpha\beta}^{\pm}$ and $[\mathcal{A}(\mathbf{k})]_{\alpha\alpha}$ are given by Eqs. (8) and (10) in the main text. We denote the expansions as

$$\begin{aligned}
Y_{\alpha\beta}^{\pm} &= Y_{0,\alpha\beta}^{\pm} + Y_{\epsilon,\alpha\beta}^{\pm}\epsilon,\\
\mathcal{A}_{\alpha\alpha} &= \mathcal{A}_{0,\alpha\alpha} + \mathcal{A}_{\epsilon,\alpha\alpha}\epsilon,
\end{aligned} \tag{B1}$$

where, for sublattices B and C, we denote $Y_{0,BC}^{+} = (2 + \Delta)\cos^2(\theta) - \Delta$, $Y_{0,BC}^{-} = (2 + \Delta)(\cos^2(\theta) - 1)$, $\mathcal{A}_{0,BB} = \mathcal{A}_{0,CC} = [-3(\Delta + 2)\cos^2(\theta)] + [3(1 + \Delta) + h]\cos(\theta)$, $Y_{\epsilon,BC}^{\pm} = (\Delta/2 + 1)(\Delta_C - \Delta_B)\sin(2\theta)$, $\mathcal{A}_{\epsilon,CC} = [-3\Delta_A + (3 + h + 3\Delta)\Delta_C]\sin(\theta) + \frac{3}{3}(2 + \Delta)(\Delta_B - \Delta_C)\sin(2\theta)$, $\mathcal{A}_{\epsilon,BB} = \mathcal{A}_{\epsilon,CC} + \Delta_{\mathrm{gap}}/\epsilon$. Then $\mathcal{A}, \mathcal{D}, \mathcal{F}$ and m in the

effective model are given by

$$\mathcal{G} = \mathcal{A}_{0,BB} + \frac{\mathcal{A}_{\epsilon,BB} + \mathcal{A}_{\epsilon,CC}}{2}\epsilon, \quad \mathcal{D} = Y^{-}_{0,BC} + Y^{-}_{\epsilon,BC}\epsilon, \quad \mathcal{F} = Y^{+}_{0,BC} + Y^{+}_{\epsilon,BC}\epsilon, \quad m = \frac{\Delta_{\text{gap}}}{2}. \tag{B2}$$

It is worth pointing out that because ϵ is a small quantity, we can ignore the second term in the definition of $\mathcal{G}$, $\mathcal{D}$, and $\mathcal{F}$ without affecting the qualitative results.

[1] A. Rycerz, J. Tworzydło, and C. Beenakker, Nat. Phys. **3**, 172 (2007).
[2] J. R. Schaibley, H. Y. Yu, G. Clark, P. Rivera, J. S. Ross, K. L. Seyler, W. Yao, and X. D. Xu, Nat. Rev. Mater. **1**, 16055 (2016).
[3] D. Xiao, W. Yao, and Q. Niu, Phys. Rev. Lett. **99**, 236809 (2007).
[4] V. T. Renard, B. A. Piot, X. Waintal, G. Fleury, D. Cooper, Y. Niida, D. Tregurtha, A. Fujiwara, Y. Hirayama, and K. Takashina, Nat. Commun. **6**, 7230 (2015).
[5] D. Xiao, G.-B. Liu, W. Feng, X. Xu, and W. Yao, Phys. Rev. Lett. **108**, 196802 (2012).
[6] Z. Yu, H. Pan, and Y. Yao, Phys. Rev. B **92**, 155419 (2015).
[7] T. Habe and M. Koshino, Phys. Rev. B **96**, 085411 (2017).
[8] H. Katsura, N. Nagaosa, and P. A. Lee, Phys. Rev. Lett. **104**, 066403 (2010).
[9] L. Zhang, J. Ren, J.-S. Wang, and B. Li, Phys. Rev. B **87**, 144101 (2013).
[10] A. Mook, J. Henk, and I. Mertig, Phys. Rev. B **89**, 134409 (2014).
[11] R. Matsumoto, R. Shindou, and S. Murakami, Phys. Rev. B **89**, 054420 (2014).
[12] S. A. Owerre, Phys. Rev. B **94**, 094405 (2016).
[13] S. A. Owerre, J. Phys.: Condens. Matter **28**, 386001 (2016).
[14] S. A. Owerre, Phys. Rev. B **95**, 014422 (2017).
[15] P. Laurell and G. A. Fiete, Phys. Rev. B **98**, 094419 (2018).
[16] K.-S. Kim, K. H. Lee, S. B. Chung, and J.-G. Park, Phys. Rev. B **100**, 064412 (2019).
[17] L. Chen, Chin. Phys. B **28**, 078503 (2019).
[18] A. Mook, J. Henk, and I. Mertig, Phys. Rev. B **99**, 014427 (2019).
[19] Z.-X. Li, Y. Cao, and P. Yan, Phys. Rep. **915**, 1 (2021).
[20] Z. Cai, S. Bao, Z. L. Gu, Y. P. Gao, Z. Ma, Y. Shangguan, W. Si, Z. Y. Dong, W. Wang, Y. Wu, D. Lin, J. Wang, K. Ran, S. Li, D. Adroja, X. Xi, S. L. Yu, X. Wu, J. X. Li, and J. Wen, Phys. Rev. B **104**, L020402 (2021).
[21] F. Zhu, L. Zhang, X. Wang, F. J. dos Santos, J. Song, T. Mueller, K. Schmalzl, W. F. Schmidt, A. Ivanov, J. T. Park *et al.*, Sci. Adv. **7**, eabi7532 (2021).
[22] A. Mook, K. Plekhanov, J. Klinovaja, and D. Loss, Phys. Rev. X **11**, 021061 (2021).
[23] Z. Zhang, W. Feng, Y. Yao, and B. Tang, Phys. Lett. A **414**, 127630 (2021).
[24] P. A. McClarty, Annu. Rev. Condens. Matter Phys. **13**, 171 (2022).
[25] R. Matsumoto and S. Murakami, Phys. Rev. Lett. **106**, 197202 (2011).
[26] Y. Onose, T. Ideue, H. Katsura, Y. Shiomi, N. Nagaosa, and Y. Tokura, Science **329**, 297 (2010).
[27] T. Ideue, Y. Onose, H. Katsura, Y. Shiomi, S. Ishiwata, N. Nagaosa, and Y. Tokura, Phys. Rev. B **85**, 134411 (2012).
[28] R. Chisnell, J. S. Helton, D. E. Freedman, D. K. Singh, R. I. Bewley, D. G. Nocera, and Y. S. Lee, Phys. Rev. Lett. **115**, 147201 (2015).
[29] M. Hirschberger, R. Chisnell, Y. S. Lee, and N. P. Ong, Phys. Rev. Lett. **115**, 106603 (2015).
[30] R. Hidalgo-Sacoto, R. I. Gonzalez, E. E. Vogel, S. Allende, J. D. Mella, C. Cardenas, R. E. Troncoso, and F. Munoz, Phys. Rev. B **101**, 205425 (2020).
[31] X. Zhai and Y. M. Blanter, Phys. Rev. B **102**, 075407 (2020).
[32] D. Ghader, Sci. Rep. **10**, 16733 (2020).
[33] D. Ghader, New J. Phys. **23**, 053022 (2021).
[34] M. Lee, E. S. Choi, X. Huang, J. Ma, C. R. Dela Cruz, M. Matsuda, W. Tian, Z. L. Dun, S. Dong, and H. D. Zhou, Phys. Rev. B **90**, 224402 (2014).
[35] R. Ishii *et al.*, Europhys. Lett. **94**, 17001 (2011).
[36] Z. Lu, L. Ge, G. Wang, M. Russina, G. Gunther, C. R. dela Cruz, R. Sinclair, H. D. Zhou, and J. Ma, Phys. Rev. B **98**, 094412 (2018).
[37] L. E. Svistov, A. I. Smirnov, L. A. Prozorova, O. A. Petrenko, A. Micheler, N. Buttgen, A. Y. Shapiro, and L. N. Demianets, Phys. Rev. B **74**, 024412 (2006).
[38] T. Ono, H. Tanaka, H. Aruga Katori, F. Ishikawa, H. Mitamura, and T. Goto, Phys. Rev. B **67**, 104431 (2003).
[39] R. Coldea, D. A. Tennant, A. M. Tsvelik, and Z. Tylczynski, Phys. Rev. Lett. **86**, 1335 (2001).
[40] R. Coldea, D. A. Tennant, K. Habicht, P. Smeibidl, C. Wolters, and Z. Tylczynski, Phys. Rev. Lett. **88**, 137203 (2002).
[41] R. Coldea, D. A. Tennant, and Z. Tylczynski, Phys. Rev. B **68**, 134424 (2003).
[42] N. A. Fortune, S. T. Hannahs, Y. Yoshida, T. E. Sherline, T. Ono, H. Tanaka, and Y. Takano, Phys. Rev. Lett. **102**, 257201 (2009).
[43] H. D. Zhou, C. Xu, A. M. Hallas, H. J. Silverstein, C. R. Wiebe, I. Umegaki, J. Q. Yan, T. P. Murphy, J.-H. Park, Y. Qiu, J. R. D. Copley, J. S. Gardner, and Y. Takano, Phys. Rev. Lett. **109**, 267206 (2012).
[44] T. Susuki, N. Kurita, T. Tanaka, H. Nojiri, A. Matsuo, K. Kindo, and H. Tanaka, Phys. Rev. Lett. **110**, 267201 (2013).
[45] G. Koutroulakis, T. Zhou, Y. Kamiya, J. D. Thompson, H. D. Zhou, C. D. Batista, and S. E. Brown, Phys. Rev. B **91**, 024410 (2015).
[46] Y. Shirata, H. Tanaka, A. Matsuo, and K. Kindo, Phys. Rev. Lett. **108**, 057205 (2012).
[47] Y. Shimizu, K. Miyagawa, K. Kanoda, M. Maesato, and G. Saito, Phys. Rev. Lett. **91**, 107001 (2003).

[48] G. Murthy, D. Arovas, and A. Auerbach, Phys. Rev. B **55**, 3104 (1997).
[49] S. Miyashita, J. Phys. Soc. Jpn. **55**, 3605 (1986).
[50] D. Yamamoto, G. Marmorini, and I. Danshita, Phys. Rev. Lett. **112**, 127203 (2014).
[51] C. Griset, S. Head, J. Alicea, and O. A. Starykh, Phys. Rev. B **84**, 245108 (2011).
[52] J. Colpa, Phys. A (Amsterdam, Neth.) **93**, 327 (1978).
[53] R. Cheng, S. Okamoto, and D. Xiao, Phys. Rev. Lett. **117**, 217202 (2016).
[54] Y.-F. Yang, G.-M. Zhang, and F.-C. Zhang, Phys. Rev. Lett. **124**, 186602 (2020).
[55] A. Sera, Y. Kousaka, J. Akimitsu, M. Sera, T. Kawamata, and Y. Koike, and K. Inoue, Phys. Rev. B **94**, 214408 (2016).
[56] J. Simon, W. S. Bakr, R. Ma, M. E. Tai, P. M. Preiss, and M. Greiner, Nature (London) **472**, 307 (2011).
[57] D.-W. Zhang, Y.-Q. Zhu, Y. X. Zhao, H. Yan, and S.-L. Zhu, Adv. Phys. **67**, 253 (2018).
[58] L.-M. Duan, E. Demler, and M. D. Lukin, Phys. Rev. Lett. **91**, 090402 (2003).
[59] J. J. García-Ripoll, M. A. Martin-Delgado, and J. I. Cirac, Phys. Rev. Lett. **93**, 250405 (2004).
[60] D. Yamamoto, T. Fukuhara, and I. Danshita, Commun. Phys. **3**, 56 (2020).